

# The Shear-to-Cosmology Paradigm I: Hybrid Field-Level and Simulation-Based Framework for Weak Lensing Surveys

JIACHENG DING <sup>1</sup>, CHEN SU <sup>1</sup>, JI YAO <sup>1</sup>, LE ZHANG <sup>2,3</sup> AND HUANYUAN SHAN <sup>1</sup>

<sup>1</sup>*Shanghai Astronomical Observatory, Chinese Academy of Sciences, Shanghai 200030, P. R. China*

<sup>2</sup>*School of Physics and Astronomy, Sun Yat-Sen University, Zhuhai 519082, P. R. China*

<sup>3</sup>*CSST Science Center for the Guangdong–Hong Kong–Macau Greater Bay Area, SYSU, Zhuhai 519082, P. R. China*

## ABSTRACT

Precise cosmological inference from next-generation weak lensing surveys requires extracting non-Gaussian information beyond standard two-point statistics. We present a hybrid machine-learning (ML) framework that integrates field-level inference (FLI) with simulation-based inference (SBI) to map observed shear fields directly to cosmological parameters, eliminating the need for convergence reconstruction. The FLI network extracts rich non-Gaussian information from the shear field to produce informative features, which are then used by SBI to model the resulting complex posteriors. To mitigate noise from intrinsic galaxy shapes, we develop a blind, training-free, PCA-based shear denoising method. Tests on CSST-like mock catalogs reveal significant performance gains. The shear-based inference achieves approximately twice the cosmological constraining power in Figure of Merit (FoM) compared to the conventional convergence-based approach. Moreover, the combination of PCA denoising and ML compression can deliver a 36.4% improvement in FoM over standard shear two-point statistics. This work establishes a scalable and robust pathway for cosmological inference, unlocking the full potential of Stage-IV weak-lensing surveys.

*Keywords:* weak lensing, shear denoising, field-level inference, simulation-based inference

## 1. INTRODUCTION

Weak lensing (WL) is a powerful probe in modern cosmology. According to General Relativity, light rays are deflected when passing through inhomogeneous matter distributions, leading to subtle distortions in the observed shapes of background galaxies. By statistically analyzing the shape distortions of millions of galaxies, one can directly map the large-scale distribution of total matter, including both dark matter and baryons, across the cosmic web. This makes WL an essential tool for constraining cosmological parameters, testing theories of gravity, and investigating the nature of dark energy (M. Kilbinger 2015; R. Mandelbaum 2018; M. Meneghetti 2022). In addition, WL-based dark matter (DM) reconstruction techniques (R. Massey et al. 2007; L. Van Waerbeke et al. 2013; H. Y. Shan et al. 2014; M. Oguri et al. 2018) and DM halo identification methods (H.

Hoekstra et al. 2004; J. Y. Tang & Z. H. Fan 2005; H. Shan et al. 2012) have played a key role in tracing the growth and spatial distribution of large-scale structures (LSS) in the Universe.

Over the past decade, Stage-III WL surveys such as DES (Dark Energy Survey Collaboration et al. 2016), KiDS, and HSC (H. Aihara et al. 2018) have mapped thousands of square degrees of the sky with dedicated pipelines and achieved 1% control of systematics, establishing a solid foundation for precision cosmology. Building on these advances, ongoing and upcoming Stage-IV surveys, including the China Space Station Survey Telescope (CSST) (J. Yao et al. 2024; CSST Collaboration et al. 2025; Y. Gong et al. 2025), Euclid (Euclid Collaboration et al. 2025), LSST (Ž. Ivezić et al. 2019), and the Roman Space Telescope (D. Spergel et al. 2015), will expand sky coverage to tens of thousands of square degrees and deliver substantially improved measurement precision, enabling unprecedented tests of dark energy, gravity, and structure formation.

Traditionally, cosmological inference has relied on two-point statistics within a Bayesian framework (Planck Collaboration et al. 2020; F. Leclercq & A. Heavens

Email:

ji.yao@shao.ac.cn,  
zhangle7@mail.sysu.edu.cn,  
hyshan@shao.ac.cn

2021; L. E. Padilla et al. 2021; P. L. Taylor & K. Marković 2022). However, several challenges become acute as data quality improves. Modeling WL observables to Stage-IV accuracy is difficult due to nonlinear gravitational evolution, baryonic effects, and complex observational systematics, including PSF modeling, survey geometry, photometric redshift errors, and intrinsic alignments (W. Hu 1999; P. Schneider et al. 2002; G. M. Bernstein 2009; T. Schrabback et al. 2010; J. Benjamin et al. 2013; J. Yao et al. 2023). Moreover, late-time cosmic fields are highly non-Gaussian, so two-point statistics capture only a fraction of the available information. Although higher-order statistics, such as peak counts, Minkowski functionals, and wavelet moments (J. P. Dietrich & J. Hartlap 2010; H. Shan et al. 2018; J. M. Kratochvil et al. 2012; A. Petri et al. 2013; S. Cheng et al. 2020, 2025), are more sensitive to nonlinear structure, only a few have robust theoretical models, limiting their practical use. These limitations have motivated a shift toward field-level inference (FLI) (F. Leclercq 2025), which operates directly on high-dimensional cosmic fields rather than compressed summary statistics. By analyzing the full fields, FLI preserves non-Gaussian information and avoids reliance on approximate analytic models of nonlinear structure. Instead, it relies on explicit forward modeling to simulate cosmological fields and observational effects, including survey masking, noise, and instrumental systematics, thereby substantially mitigating the challenges posed by complex data models (F. Leclercq & A. Heavens 2021; S. Stopyra et al. 2024).

Machine learning (ML) techniques are increasingly applied in cosmological data processing and analysis (S. Dieleman et al. 2015; C. E. Petrillo et al. 2017; K. Schawinski et al. 2017; Z. Zhang et al. 2024; T. Liu et al. 2025; Y. Wu et al. 2025; F. Zhong et al. 2025). In cosmological FLI, ML can learn the complex nonlinear mapping between cosmological parameters and high-dimensional fields directly from simulations, greatly reducing the computational cost of traditional FLI (J. Fluri et al. 2019; H. J. Hortúa et al. 2020; Z. Min et al. 2024). Furthermore, building on the ML-driven framework, simulation-based inference (SBI) offers a likelihood-free approach that learns the full posterior distribution of cosmological parameters from simulated observables (K. Cranmer et al. 2020; P. Lemos et al. 2023; C. Su et al. 2025; J. Zeghal et al. 2025). By leveraging the forward model, SBI naturally incorporates nonlinear evolution and observational systematics, overcoming the limitations of Gaussian-likelihood assumptions and the inefficiency of MCMC sampling in high-dimensional spaces. Consequently, ML-driven SBI has emerged as a scalable

and accurate methodology for extracting cosmological information from Stage-IV WL surveys.

In WL cosmology, previous studies have primarily extracted cosmological information from the convergence field (A. Petri et al. 2013; H. Shan et al. 2018; J. Fluri et al. 2022; T. Lu et al. 2023) by analyzing its morphology, topology, and peak statistics (J. Liu & Z. Haiman 2016). However, the convergence field is not directly observable and must be reconstructed from the measured shear, a process sensitive to the reconstruction algorithm and often degraded by complex survey masks. Additionally, shear measurements involve multiple calibration and correction steps that can introduce systematic uncertainties propagating into the convergence field. To mitigate these effects, this work applies FLI directly to shear fields, while also comparing results with convergence-based inference.

In shear measurements, the dominant noise arises from the intrinsic shapes of galaxies. While intrinsic alignments (IA) induce correlations, these are largely confined to galaxies within the same redshift slice. As a result, the shear signal varies smoothly with redshift, whereas shape noise exhibits stochastic, non-smooth fluctuations. To exploit this property, we perform principal component analysis (PCA) on noisy shear maps across multiple redshift slices: the smooth, coherent components capture the underlying shear signal, while the rapidly fluctuating components correspond to random shape noise. This denoising procedure requires no explicit modeling, analogous to blind-analysis methods commonly used in 21 cm intensity mapping (D. Alonso et al. 2015).

In this work, we develop a shear-to-cosmology framework, enabling more direct, information-efficient, and statistically optimal use of the data, particularly in the presence of complex survey geometries. Section 2 presents the methodological framework, including the FLI network and SBI strategy. Section 3 describes the mock pipeline for generating shear fields. Section 4 details shear denoising and convergence reconstruction. Section 5 presents the inference results, comparing shear- and convergence-based estimates and demonstrating the improvements from PCA denoising. Section 6 summarizes the main findings.

## 2. METHODOLOGY

The hybrid inference framework, illustrated in Figure 1, consists of two main components:

1. a FLI network (inside the dashed box), trained to map WL shear fields to cosmological parameters, for generating informative feature representations;

2. a SBI module (outside the dashed box) that estimates posteriors from summary statistics, either using conventional shear two-point correlation functions (2PCFs) or ML-derived features.

### 2.1. Field-Level Inference Network

FLI refers to statistical methods that extract physical fields and cosmological parameters directly from observed data, with the likelihood defined over the entire discretized field and without compressing the map-level information. Neural network can be considered a realization of FLI: it can encode latent representations while still enabling a near-direct mapping from the physical fields to cosmological parameters.

#### 2.1.1. Input Data

As shown in Figure 1, the input sample is a six-dimensional shear field, including the 4 sky blocks across 16 photo- $z$  slices. Its shape is  $(B, N_\gamma, N_z, N_{\text{blk}}, H, W) = (B, 2, 16, 4, 64, 64)$ , where  $B$  is the batch size,  $N_\gamma$  the shear components,  $N_z$  the photo- $z$  slices,  $N_{\text{blk}}$  the input sky blocks within each sky group, and  $(H, W)$  the spatial map size. Along the redshift direction, the 16 photo- $z$  slices are produced by the denoising procedure (see Section 4.1), starting from the 4 photo- $z$  bins of the CSST-like lensing sample (see Section 3.3) and covering the range  $0 < z < 4$ . From the sky-region perspective, each input sky block ( $6.4 \times 6.4 \text{ deg}^2$ ) is constructed using two data-augmentation operations applied to the original  $12.8 \times 12.8 \text{ deg}^2$  sky blocks with a resolution of  $0.1 \text{ deg/pixel}$  (see Figure 4). The first operation is random cropping, which increases the spatial diversity of the training samples by a factor of  $64^2$ . The second is random masking, where multiple circular masks with varying radii, allowed to overlap, are applied to mimic realistic survey masks. For convergence-based inference, the corresponding convergence maps are subsequently reconstructed from the prepared shear fields using the KS algorithm (section 4.2).

#### 2.1.2. Network Structure

The proposed FLI network (dashed box in Figure 1) is composed of four key components that collaboratively extract cosmological information directly from the WL shear fields.

- a. **Redshift-direction Embedding Layer:** The 3D convolutional layers with kernels elongated along the redshift axis capture the shear evolution across photo- $z$  slices.

- b.  $\gamma_1$  &  $\gamma_2$  **Merging Layer:** A Transformer block, utilizing the multi-head attention mechanism, is employed to integrate the two shear components.

- c. **Transformer-based Encoders:** Unlike conventional convolutional encoders, the Transformer (TransF)-based layer captures both local and global dependencies, naturally integrating multi-scale information across redshift slices and sky positions, thereby producing a more informative latent space for cosmological inference.

- d. **Inference layers:** For each cosmological parameter, the inference layer consists of two fully connected layers predicting the posterior mean and log-variance. The layers are intentionally kept shallow to facilitate the subsequent SBI in decoding the latent vectors.

Together, these layers enable a direct and flexible mapping from observed shear fields to cosmological parameters.

To assess the impact of convergence reconstruction on cosmological inference, we apply the shear-based FLI network to convergence data. Since the network expects two-component inputs, we duplicate the convergence map to form a compatible two-component input  $(\kappa, \kappa)$ . This setup enables a direct comparison between shear- and convergence-based inputs while keeping the network architecture and training procedure identical, isolating the effect of input type on inference performance and providing insight into the information loss in reconstructed convergence maps relative to the original shear maps.

#### 2.1.3. Loss Function

The network can directly output the posterior distributions of the cosmological parameters, specifically, the means  $\mu_i$ , log-variances  $\log \sigma_i$ , and samples  $\theta_i$  obtained via reparameterization from these posteriors. Based on this formulation, the explicit form of the loss function is given by

$$L_{\text{tot}} = \sum_{i=1}^{N_\theta} \left( \underbrace{\left( \theta_i - \hat{\theta}_i \right)^2}_{L_{\text{inf}}} + \underbrace{\frac{\beta}{2} \left( \mu_i^2 + \sigma_i^2 - \log \sigma_i^2 - 1 \right)}_{L_{\text{KL}}} \right) \quad (1)$$

where  $\hat{\theta}_i$  denotes the ground-truth cosmological parameters and  $N_\theta$  is the dimensionality of the target parameter space. The total loss  $L_{\text{tot}}$  comprises an inference loss  $L_{\text{inf}}$ , which penalizes the deviation between

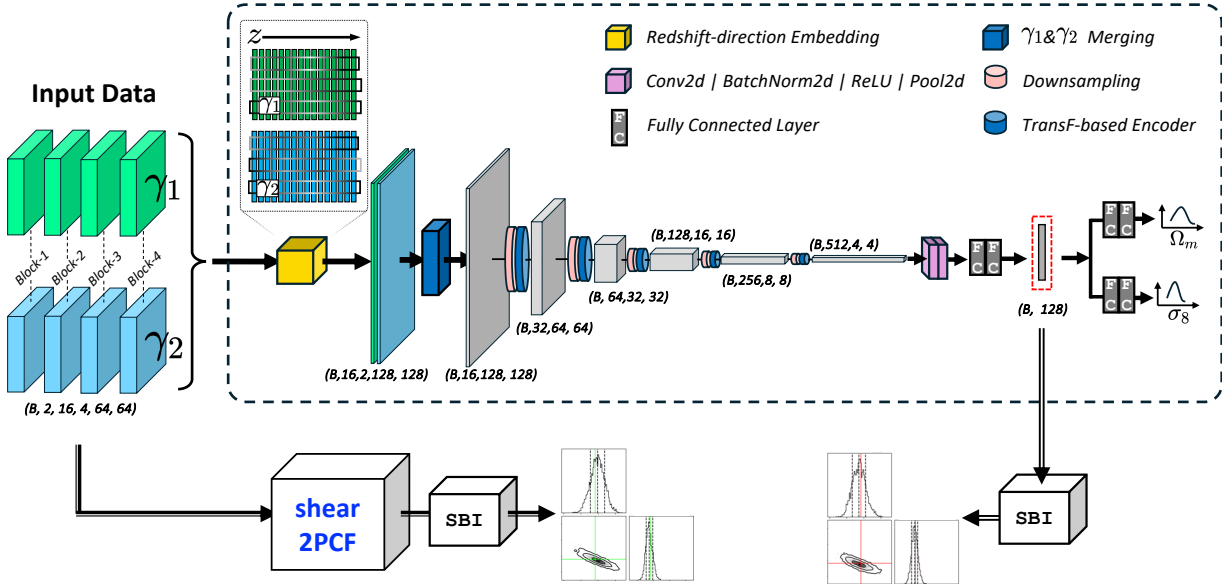


**Figure 1.** Schematic overview of the proposed framework, consisting of: **1.** a field-level inference (FLI) network (inside the dashed box) and **2.** a simulation-based inference (SBI) module (outside the dashed box). The field-level shear input is a six-dimensional tensor with shape  $(B, N_\gamma, N_z, N_{\text{blk}}, H, W) = (B, 2, 16, 4, 64, 64)$ , where  $B$  is the batch size,  $N_\gamma$  the shear components,  $N_z$  the number of photo- $z$  slices,  $N_{\text{blk}}$  the number of blocks in each sky group (see Figure 4), and  $(H, W)$  the spatial map size. The FLI network comprises four components: (a) a redshift-direction embedding layer, (b) a  $\gamma_1$  &  $\gamma_2$  merging layer, (c) Transformer (TransF)-based encoders, and (d) fully connected inference layers to predict  $(\Omega_m, \sigma_8)$ . In parallel, SBI is applied either to the ML-derived feature representation (red dashed box) or to conventional two-point statistics (2PCF). The same structure of FLI network is applied to convergence map ( $\kappa$ ) by duplicating it to form a two-component input  $(\kappa, \kappa)$ .

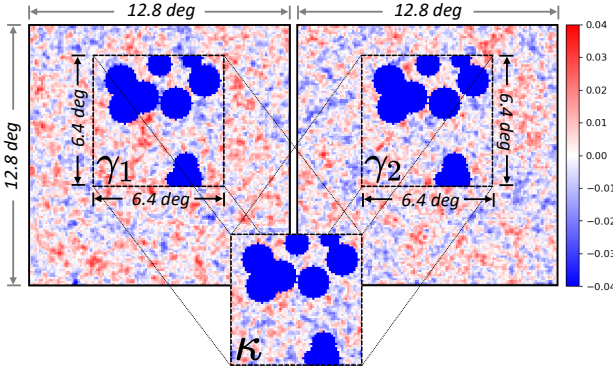


**Figure 2.** Preparation of an input sky block for training the FLI network. At a resolution of  $0.1 \text{ deg/pixel}$ , based on the original  $12.8 \times 12.8 \text{ deg}^2$  blocks, we generate  $6.4 \times 6.4 \text{ deg}^2$  inputs via two augmentations: (1) random cropping (boosting spatial diversity by  $64^2$ ), (2) random masking with overlapping circular masks to mimic survey masks. The corresponding convergence field can then be reconstructed from the prepared shear using the KS algorithm.

the predicted and ground-truth parameters, and a Kullback–Leibler (KL) divergence term  $L_{\text{KL}}$ , which regularizes the latent posterior distribution by encouraging it to approximate a standard Gaussian. To balance these two parts, a weighting hyperparameter  $\beta$  is introduced to control the contribution of the KL term, and is set to 0.01 in our experiments. During the training of the

neural network, the validation set is strictly excluded from all parameter updates. It is used solely to monitor the loss and automatically adjust the learning rate when the validation loss plateaus or worsens. Consequently, the evolution of the validation loss provides a direct indication of the model’s performance and training progress. Notably, to evaluate both the shear-based and convergence-based datasets, we employed the same network architecture as mentioned in section 2.1.

## 2.2. Simulation-Based Inference

Simulation-based inference (SBI) is a Bayesian framework for parameter estimation when the likelihood is intractable but forward simulations are available. It trains neural density estimators on simulated parameter–observation pairs to approximate the posterior. The workflow typically first compresses the forward-modeling maps or summary statistics into a low-dimensional feature space using a neural network, and then trains a conditional density model, often a normalizing flow, to relate these features to the target parameters. Once trained, the model provides an amortized posterior estimator applicable to any (mock) observation for efficient inference. We employ the `sbi`<sup>4</sup>

<sup>4</sup> <https://sbi-dev.github.io/sbi>



library (A. Tejero-Cantero et al. 2020; J. Boelts et al. 2024) and implement the Neural Posterior Estimation (NPE) technique to perform SBI.

In this paper, from the perspective of SBI, the FLI module (Figure 1) can be interpreted as a data-compression process that encodes the full WL shear field into a low-dimensional but fully informative summary statistics. Another popular summary statistic for the shear field is the shear-shear correlations. In the following sections, we compare the constraining power of these two types of summary statistics and demonstrate the significant improvements achieved through ML-based compression.

### 2.2.1. Summary Statistics: ML-derived Feature Representations

As illustrated in Figure 1, our neural network compresses each shear map into a 128-element feature Representation ( $\mathbf{x}_{\text{ML}}$ ). The extracted features depend on the network’s architecture and training scheme. In this work, the network is specifically tailored for cosmological inference and optimized with an appropriate loss function, ensuring that the compressed representation preserves maximal information relevant for constraining cosmological parameters. For the convergence-based network, we adopt the same architecture as in the shear case but train it independently, enabling the network to transform each convergence map into a representation of the same length (128).

### 2.2.2. Summary Statistics: Shear 2PCFs

In the traditional statistics of cross- $z$  2PCFs, the shear data originally consist of 16 photo- $z$  slices. To reduce the computational cost, adjacent slices are averaged to produce 8  $z$ -slices, resulting in 36 distinct pairs. For each pair  $(a, b)$ , the correlation functions are defined as

$$\xi_+^{(a,b)}(\vartheta) = \langle \gamma_t^a \gamma_t^b \rangle(\vartheta) + \langle \gamma_\times^a \gamma_\times^b \rangle(\vartheta), \quad (2)$$

$$\xi_-^{(a,b)}(\vartheta) = \langle \gamma_t^a \gamma_t^b \rangle(\vartheta) - \langle \gamma_\times^a \gamma_\times^b \rangle(\vartheta), \quad (3)$$

where  $\gamma_t$  and  $\gamma_\times$  denote the tangential and cross components of the shear, respectively. Based on TreeCorr<sup>5</sup> (M. Jarvis et al. 2004; M. Jarvis 2015) library, the measurements are performed over angular scales in the range  $\vartheta_{\min} = 6$  to  $\vartheta_{\max} = 120$ , sampled at  $N_\vartheta = 5$  logarithmically spaced points. To combine the information from all  $z$ -slice pairs, we first stack the  $\xi_+$  and  $\xi_-$  measurements across different pairs,

$$\hat{\xi}_+ = \text{stack}(\xi_+^{p1}, \xi_+^{p2}, \dots, \xi_+^{p36}), \quad (4)$$

$$\hat{\xi}_- = \text{stack}(\xi_-^{p1}, \xi_-^{p2}, \dots, \xi_-^{p36}), \quad (5)$$

and subsequently concatenate the two to construct the summary statistics,  $\hat{\xi}_{+-} = \text{stack}(\hat{\xi}_+, \hat{\xi}_-)$  with length of 360.

Although the traditional statistics ( $\hat{\xi}_{+-}$ ) involve larger data volumes than ML-derived features, subsequent SBI results show that the latter capture richer cosmological information and yield tighter parameter constraints.

## 3. MOCK PIPELINE

### 3.1. $N$ -body Simulation

To generate weak lensing maps for training and validation, we use the publicly available COSMOGRIDV1<sup>6</sup> simulation suite (T. Kacprzak et al. 2022; J. Fluri et al. 2022), which provides a diverse set of cosmologies suitable for Stage-IV lensing survey conditions. The mock catalogs are constructed to match the typical redshift distribution and galaxy number density expected in forthcoming wide-field lensing surveys (e.g., CSST, Euclid, Roman).

COSMOGRIDV1 contains 2,500 cosmologies sampled within the  $w$ CDM framework, varying  $\Omega_m$ ,  $\sigma_8$ ,  $w_0$ ,  $n_s$ ,  $\Omega_b$ ,  $h_0$ , and assuming three degenerate neutrinos with a fixed mass sum  $\sum m_\nu = 0.06$  eV. For each cosmology, seven realizations with different initial conditions were produced. The full suite includes cosmologies drawn from both wide- and narrow-grid priors. In this work, we use only the “run0” realization of 1,260 cosmologies sampled from the narrow-grid prior, spanning the parameter ranges  $\Omega_m \in [0.15, 0.45]$ ,  $\sigma_8 \in [0.5, 1.3]$ ,  $w_0 \in [-1.25, -0.75]$ ,  $n_s \in [0.93, 1.00]$ ,  $\Omega_b \in [0.04, 0.05]$ , and  $h_0 \in [0.65, 0.75]$ . Based on estimates from two-point statistics ( $\partial C_\ell / \partial \theta(\ell)$ ), (J. Yao et al. 2024), the four parameters of  $(n_s, h_0, w_0, \Omega_b)$  highly depend on angular sensitivity across over two orders of angular scales, which is limited by our “6 arcmin” small-scale cut due to the simulation limit. Therefore, as a proof of methodology, we focus on  $(\Omega_m, \sigma_8)$  to represent the cosmological constraining power in this work.

Based on the DM simulation snapshots, COSMOGRIDV1 also provides projected full-sky DM lightcone shells covering the redshift range  $0 < z < 4$ , stored in HEALPix format with resolutions of  $N_{\text{side}} = 512$  or 1024. Owing to computational limitations, we use the  $N_{\text{side}} = 512$  shells as the basis for the ray-tracing procedure to generate the weak lensing signals in this work.

### 3.2. Ray-tracing

Utilizing the  $\sim 68$  redshift shells provided in the COSMOGRIDV1 data covering the redshift interval of

<sup>5</sup> <https://rmjarvis.github.io/TreeCorr>

<sup>6</sup> <http://www.cosmogrid.ai>

$z \in [0, 4]$ , we employ the full-sky ray-tracing algorithm DORIAN<sup>7</sup> (F. Ferlito et al. 2024) to generate WL shear signals at the followed 23 redshifts:  $z \in \{0.20, 0.30, 0.40, 0.50, 0.60, 0.70, 0.80, 0.90, 1.00, 1.10, 1.20, 1.30, 1.40, 1.50, 1.60, 1.70, 1.80, 2.00, 2.20, 2.40, 2.80, 3.20, 3.60\}$ .

Notably, the simulation timesteps are not fully synchronized across different cosmologies, leading to discrepancies in the redshift sampling of the DM lightcone shells, especially at high redshifts. Such inconsistencies can introduce systematic errors and spurious features into the machine learning dataset. To address this, we adopt a coarser redshift sampling for the shear fields in the high-redshift regime, which both mitigates potential systematics and better matches the expected galaxy distributions in WL surveys, while substantially reducing computational costs.

### 3.3. Survey Setup

To validate the hybrid framework under realistic conditions, we employ mock photo- $z$  galaxy catalogs with specifications comparable to high-precision surveys such as CSST. These mocks include galaxy shape noise and irregular survey masking to emulate the observational conditions expected in large-scale weak-lensing programs.

WL shear measurements rely on accurately determining galaxy ellipticities. In theory, the observed ellipticity ( $\varepsilon$ ) of a galaxy can be approximated as a linear combination of its intrinsic ellipticity ( $\varepsilon^s$ ) and the lensing shear ( $\gamma$ ), given by

$$\varepsilon = \frac{\varepsilon^s + \gamma}{1 + \varepsilon^s \gamma^*} \quad (6)$$

where  $\gamma = \gamma_1 + \gamma_2 i$ ,  $\varepsilon^s = \varepsilon_1^s + \varepsilon_2^s i$  and “ $i$ ” denotes the imaginary unit. It is assumed that the two components of  $\varepsilon^s$  follow a Gaussian distribution with standard deviation  $\sigma_e = 0.288$ , consistent with the value adopted in the KiDS survey (H. Hildebrandt et al. 2020; C. Blake et al. 2020). Ideally, the ensemble average of galaxy ellipticities can provide an unbiased shear estimator, with  $\langle \varepsilon^s \rangle = 0$  and  $\gamma = \langle \varepsilon \rangle$ . In practice, however, the accuracy is limited by the finite surface density of usable source galaxies: insufficient samples leave residual contributions from intrinsic shapes, introducing galaxy shape noise into the WL signal. The third-generation surveys typically achieve galaxy number densities of approximately 10–20 gal/arcmin<sup>2</sup>, whereas upcoming or ongoing fourth-generation surveys are expected to reach densities as high as about 30 gal/arcmin<sup>2</sup>. China Space

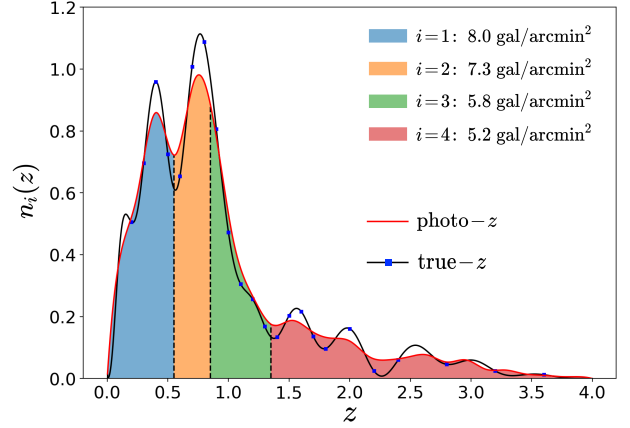


**Figure 3.** CSST-like photo- $z$  distribution. The red curve shows the photo- $z$  distribution with photo- $z$  uncertainties  $\sigma(z) = \sigma_z(1+z)$ ,  $\sigma_z = 0.05$ . Using this  $z$ -dependent kernel, the true- $z$  distribution (marked curve) is obtained by deconvolution. A mock true- $z$  galaxy catalog is generated assuming a galaxy number density of 26 gal/arcmin<sup>2</sup> and intrinsic shape noise  $\sigma_e = 0.288$ . Incorporating photo- $z$  uncertainties, the mock photo- $z$  catalog is then constructed. To enhance the S/N of the WL signal, the photo- $z$  catalog is divided into 4  $z$ -bins, each shown in a different color with its corresponding galaxy number density.

Station Survey Telescope (CSST) is a Stage-IV space-based observatory for wide-field photometric imaging and slitless spectroscopy, targeting a sky coverage of 17,500 deg<sup>2</sup> (Y. Cao et al. 2018; Y. Gong et al. 2019; H. Zhan 2021). Its upcoming WL survey is expected to achieve a galaxy number density of  $\sim 26$  gal/arcmin<sup>2</sup> (Y. Gong et al. 2019; Z. Liu et al. 2024).

Cropping shear maps from full-sky HEALPix maps at different redshifts yields a series of pure multi-redshift shear maps. To generate the mock WL catalog, galaxies are placed at the centers of the corresponding mesh pixels, ignoring their finer spatial distribution within each pixel. Based on the photometric-redshift (photo- $z$ ) distribution of CSST lensing samples (J. Yao et al. 2024), a CSST-like catalog can then be generated through the following steps.

- (1) We adopt the photo- $z$  distribution of CSST lensing galaxies (red curve in Figure 3), assuming a photo- $z$  uncertainty parameterized as  $\sigma(z) = \sigma_z(1+z)$ , with  $\sigma_z = 0.05$  (Y. Cao et al. 2018). The corresponding true- $z$  distribution is then recovered through a deconvolution procedure.
- (2) Using the recovered true- $z$  distribution (black curve in Figure 3) and an assumed galaxy number density of 26 gal/arcmin<sup>2</sup>, we generate a

<sup>7</sup> <https://gitlab.mpcdf.mpg.de/ferlito/dorian>

mock sample of galaxies with redshifts drawn accordingly.

- (3) Finally, by assigning shear signals from simulated shear fields at multiple redshifts (blue squares in Figure 3) and incorporating intrinsic shape noise with a dispersion of  $\sigma_e = 0.288$ , we construct the CSST-like photo- $z$  galaxy catalog.

As a preliminary investigation within the shear-to-cosmology framework, this work focuses solely on extracting cosmological information in the presence of galaxy shape noise and photo- $z$  uncertainties, deferring the inclusion of PSF effects, shear measurement biases, mean redshift biases, intrinsic alignments (IA), baryonic feedback, reduced shear, source clustering, magnification, and other systematics to future studies using larger simulation sets.

#### 4. DATA PREPROCESSING

The goal of employing FLI is to maximally extract the non-Gaussian information encoded in the data. Conventional smoothing operations inevitably suppress such features, motivating the development of denoising techniques tailored to FLI. These approaches aim to reduce noise while preserving the essential non-Gaussian structure of the field. Moreover, improving the pixel-level S/N ratio further enhances the fidelity and constraining power of field-level analyses. Machine-learning approaches, such as GAN-based models (M. Shirasaki et al. 2021) and diffusion models (S. D. Aoyama et al. 2025), have been applied to WL mass maps. In contrast, our goal is to develop a blind, training-free denoising technique that requires no learned model, which forms a key methodological component of this work.

##### 4.1. Shear Denoising

The entire mock galaxy catalog over the entire photo- $z$  range is divided into 4 photo- $z$  bins, as shown in Fig. 3. Considering both the photo- $z$  distribution of CSST galaxies and the characteristic decline of WL strength at lower redshifts, the number of galaxies in the low photo- $z$  bins is appropriately increased to boost the WL signal in those bins.

For each sky block in Fig. 4, the shear data can be obtained through the following steps (illustrated in Figure 5), incorporating analytical operations to suppress noise and enhance the shear signal quality.

- (a) **Subdivision:** Within each photo- $z$  bin and sky block, galaxies are further divided into 8 subsets based on their photo- $z$  values, in preparation for the denoising operation described below. In each subset, we calculate the noisy

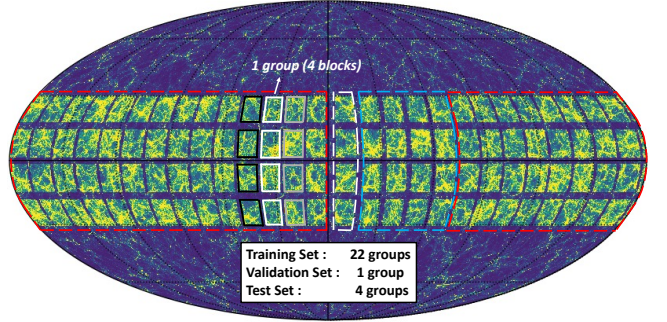


**Figure 4.** Illustration of the sky-region partitioning into training, validation, and test sets. For each cosmology, the dataset contains 108 sky blocks, grouped in fours within the same declination region. Groups enclosed by red, blue, and white dashed boxes indicate the training, test, and validation sets, respectively, with no overlapping sky regions. Each block is a  $128 \times 128$  mesh spanning  $12.8 \times 12.8 \text{ deg}^2$  and is randomly cropped to  $6.4 \times 6.4 \text{ deg}^2$  before input to the neural network. Each group of cropped blocks forms a sample, covering  $163.84 \text{ deg}^2$ .

shear maps ( $\gamma^{\text{ns}}$ ) by averaging the galaxy ellipticities, expressed as

$$\gamma^{\text{ns}} = \langle \epsilon \rangle. \quad (7)$$

Notably, we adopt the simplified precondition here that all galaxies reside entirely within pixel boundaries, neglecting the complexities associated with those intersecting pixel edges.

- (b) **Multi-Smoothing:** The noisy shear map in each subset is smoothed with a set of Gaussian kernels,

$$\begin{aligned} \gamma^{\text{sm}}(\theta) &= [\gamma^{\text{ns}} \otimes \mathcal{G}](\theta) \\ &\Rightarrow \tilde{\gamma}^{\text{sm}}(\ell) = \tilde{\mathcal{G}}(\ell) \cdot \tilde{\gamma}^{\text{ns}}(\ell) \end{aligned} \quad (8)$$

where the Gaussian kernel in Fourier space is given by

$$\tilde{\mathcal{G}}(\ell) := \exp\left(-\frac{|\ell|^2}{2\tilde{\sigma}_{\text{sm}}^2}\right). \quad (9)$$

Here we adopt a set of smoothing scales in Fourier space,  $\tilde{\sigma}_{\text{sm}} = [10, 20, 40] \text{ pixel}^{-1}$ , which correspond to Gaussian kernel widths in real space of  $\sigma_{\text{sm}} = [1.00, 0.50, 0.25] \text{ deg}$ , respectively. Intuitively, feeding multiple independently smoothed results into a neural network preserves multi-scale, non-Gaussian features. Although increased smoothing improves the S/N ratio, it reduces local complexity, making overfitting more likely. Averaging multiple smoothed results may offer a balance between

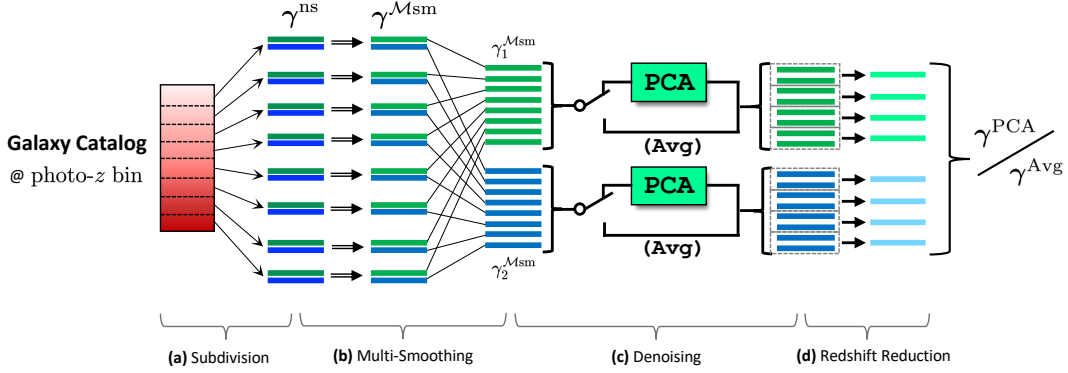


**Figure 5.** Pipeline of shear measurement in each photo- $z$  bin including 4 steps to enhance the shear signal quality. When PCA processing is applied, the denoised shear field is denoted as  $\gamma^{PCA}$ ; otherwise, the resulting field is denoted as  $\gamma^{Avg}$ .

information retention and overfitting prevention, expressed as

$$\gamma^{Msm}(\theta) = \frac{1}{N_{sm}} \sum_{n=1}^{N_{sm}} \gamma^{sm}(\theta). \quad (10)$$

- (c) **Denoising:** Conventional denoising algorithms (like smoothing and Wiener-filter) normally down-weight the high- $\ell$  modes at map-level, while ignoring the fact that shear signals are not. Based on the resulting  $\gamma^{Msm}$  from 8 subsets, one can further suppress the noise level via the denoising algorithm – Principal Component Analysis (PCA):

$$\begin{bmatrix} \gamma_{(1)}^{PCA} \\ \gamma_{(2)}^{PCA} \\ \dots \\ \gamma_{(8)}^{PCA} \end{bmatrix} = \text{PCA} \left( \begin{bmatrix} \gamma_{(1)}^{Msm} \\ \gamma_{(2)}^{Msm} \\ \dots \\ \gamma_{(8)}^{Msm} \end{bmatrix} \right). \quad (11)$$

Based on the PCA decomposition, the input shear data are separated into 8 orthogonal modes. We retain only the first 2 smooth principal components for shear reconstruction, since the true shear field varies smoothly with redshift, whereas the shape noise manifests as random fluctuations.

- (d) **Redshift Reduction:** Combining the outputs from the 4 photo- $z$  bins yields a four-dimensional shear dataset ( $N_\gamma = 2$ ,  $N_z = 32$ ,  $H$ ,  $W$ ), where  $N_\gamma$  and  $N_z$  denote the two shear components and the redshift dimension after denoising, respectively. To reduce its data size for ML or statistical analyses, every two consecutive redshift layers are averaged, resulting in ( $N_\gamma = 2$ ,  $N_z = 16$ ,  $H$ ,  $W$ ). The processed

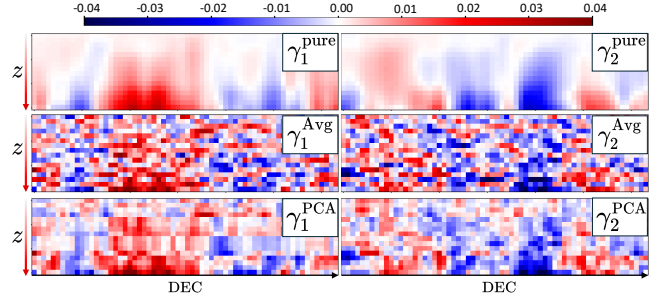


**Figure 6.** Visualization of shear denoising. The bottom panels show shear fields from the pipeline in Figure 5 including PCA denoising ( $\gamma^{PCA}$ ), while the middle panels show shear fields from the pipeline without PCA ( $\gamma^{Avg}$ ). The top panels display the corresponding pure shear signals after the same multi-smoothing operation ( $\gamma^{pure}$ ). In each panel, the horizontal axis corresponds to declination and the vertical axis to redshift. As shown in the figure, PCA denoising clearly preserves more reliable redshift structures, which provide the key information for our inference framework.

data is denoted as  $\gamma^{PCA}$  when PCA is applied, and  $\gamma^{Avg}$  otherwise.

It is worth noting that we employed a small trick: the mask effect is applied to the prepared shear maps ( $\gamma^{PCA}$  or  $\gamma^{Avg}$ ). Although this treatment does not fully correspond to the actual mask, it can significantly accelerate the training of the neural network.

#### 4.2. Convergence Mapping

Based on the prepared shear field ( $\gamma^{PCA}$  or  $\gamma^{Avg}$ ), generated with random masks during training, we apply the KS algorithm (N. Kaiser & G. Squires 1993) to reconstruct the convergence field ( $\kappa$ ), retaining only its



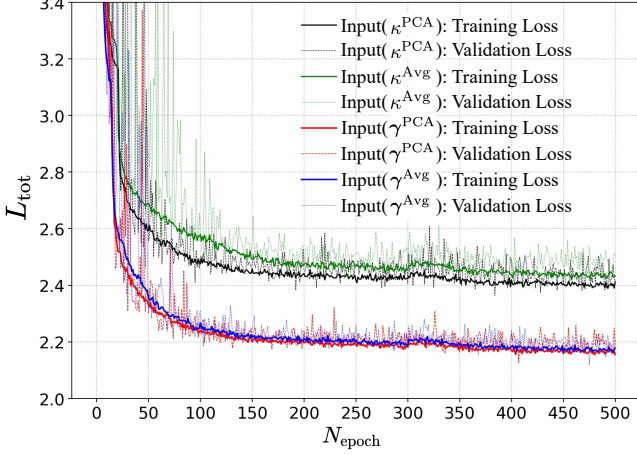


**Figure 7.** Evolution of the loss (batch size = 32) for different input data: the shear maps  $\gamma^{\text{PCA}}$  (with denoising) and  $\gamma^{\text{Avg}}$  (without denoising), the corresponding convergence maps  $\kappa^{\text{PCA}}$  and  $\kappa^{\text{Avg}}$  via KS algorithm. In neural network training, the validation set is excluded from parameter optimization and serves solely to trigger automatic learning rate reduction based on variations in its loss. Consequently, the evolution of validation loss reflects the model’s performance improvement.

E-mode component:

$$\begin{aligned} \kappa^{\text{prep}}(\theta) &\leftarrow \text{KS}(\gamma^{\text{prep}}(\theta)): \\ \tilde{\kappa}^{\text{prep}}(\ell) &= D^*(\ell) \tilde{\gamma}^{\text{prep}}(\ell), \\ D(\ell) &= \frac{\ell_1^2 - \ell_2^2 + 2i\ell_1\ell_2}{|\ell|^2}, \end{aligned} \quad (12)$$

where  $D(\ell)$  is the projection operator, “i” denotes the imaginary unit, and the option “prep” can be specified as “PCA” or “Avg”.

## 5. RESULTS

### 5.1. Loss Evolution

As illustrated in Figure 6, PCA denoising effectively enhances the S/N ratio of the shear data and further reduces the training loss. To evaluate its impact, we compare the FLI results with and without PCA denoising. Based on the loss function described in Sec. 2.1.3, Figure 7 presents the training loss evolution with a batch size of 32 for four types of input data. The first two are convergence fields, the averaged convergence ( $\kappa^{\text{Avg}}$ ) and the PCA-denoised convergence ( $\kappa^{\text{PCA}}$ ), both reconstructed from their corresponding shear fields using the KS algorithm. The other two are shear fields: the averaged shear ( $\gamma^{\text{Avg}}$ ) and the PCA-denoised shear ( $\gamma^{\text{PCA}}$ ). As shown in Figure 7, the shear-based approaches achieve substantially lower losses than the convergence-based ones, since convergence reconstruction introduces additional systematic errors, particularly in the presence of sky masking.

### 5.2. Predictions by FLI

Under the assumption of Gaussian distribution, the trained FLI network can output the posteriors of the target parameters ( $\Omega_m$ ,  $\sigma_8$ ) directly. As shown in Figure 4 in Appendix, the prepared test set includes 4 discrete sky groups per cosmology, covering a total of  $655.36 \text{ deg}^2$ . In order to highlight the differences between the input data types: ( $\gamma^{\text{Avg}}$ ,  $\gamma^{\text{PCA}}$ ,  $\kappa^{\text{Avg}}$ ,  $\kappa^{\text{PCA}}$ ), we average the FLI predictions from the 4 sky groups for each cosmology in Figure A1. As shown in the figure, qualitatively, shear-based inference outperforms convergence-based inference. Furthermore, applying PCA denoising reduces the systematic bias of the predictions relative to the true values.

### 5.3. Validation of Predictions

Probability Integral Transform (PIT) is a standard diagnostic tool for evaluating the reliability of model-predicted probability distributions. When a model’s cumulative distribution function (CDF) is well calibrated, the PIT values obtained by evaluating observed data against the CDF follow a uniform distribution. PIT thus offers a simple yet effective way to assess both the calibration and uncertainty of probabilistic predictions.

In this work, cosmological parameters are inferred using two approaches: (1) directly from the FLI network, and SBI applied to summary statistics. We perform PIT analyses on the posteriors obtained from both methods to evaluate their inference quality and provide an additional consistency check for our framework.

As shown in Figure 8, the PIT distributions from SBI are noticeably closer to uniform than those from the FLI network, indicating better-calibrated posteriors. This is expected because, although both methods use the same ML-derived feature representations, the inference module in the FLI network, comprising fully connected layers (Figure 1), assumes Gaussian posteriors, which limits its flexibility and accuracy. In contrast, SBI directly learns the mapping from features to parameter posteriors using simulated data, enabling it to capture complex, non-Gaussian, and even multi-modal distributions. By explicitly modeling the full posterior, SBI naturally accounts for parameter correlations and uncertainties, yielding more reliable and accurate inference than the Gaussian-constrained network outputs.

### 5.4. Cosmological Outputs

Simulation-based inference (SBI) offers a flexible and statistically rigorous framework for cosmological parameter estimation from complex data. In this study, we employ two distinct forms of summary statistics: (1) ML-derived feature representation ( $x_{\text{ML}}$ ) and (2) the

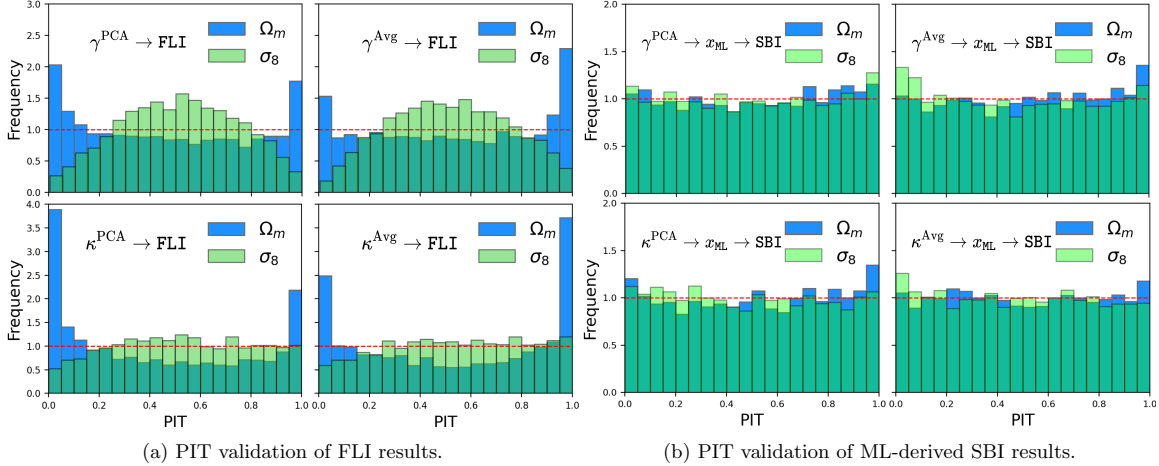


**Figure 8.** Comparison of PIT validation results between field-level inference (FLI) and ML-derived simulation-based inference (SBI), performed using four types of input data: ( $\gamma^{\text{PCA}}$ ,  $\gamma^{\text{Avg}}$ ,  $\kappa^{\text{PCA}}$ ,  $\kappa^{\text{Avg}}$ ). Compared with FLI, the PIT distribution of SBI is closer to a uniform distribution, indicating that the SBI posteriors are better calibrated and more consistent with the true parameters.

shear 2PCF ( $\hat{\xi}_{+-}$ ). The constraining power on the target cosmological parameters is quantified by the Figure of Merit (FoM), normalized per square degree. Due to the inherent randomness in SBI training, we perform 10 independent SBI runs for each case and select the model with the strongest constraining power. To demonstrate the SBI performance in each case, we adopt the fiducial cosmology characterized by  $(\Omega_m^{\text{true}}, \sigma_8^{\text{true}}) = (0.3062, 0.7615)$ .

Figure 9 presents the posterior distributions inferred from three SBI schemes, all applied to PCA-denoised weak lensing fields. The left panel shows the results based on 2PCF summaries derived from the PCA-denoised shear field ( $\gamma^{\text{PCA}}$ ), whereas the middle and right panels correspond to ML-derived features extracted from the PCA-denoised convergence ( $\kappa^{\text{PCA}}$ ) and shear ( $\gamma^{\text{PCA}}$ ), respectively. A comparison between the left and right panels reveals that ML-derived features enhance the parameter constraining power by 29.3% relative to the 2PCF-based summaries. Moreover, the shear-based ML representation outperforms its convergence-based counterpart by 99.0%, highlighting the richer cosmological information retained in the shear domain.

To further assess the impact of PCA denoising on shear-field-based posterior inference, we compare the results of 2PCF-based and ML-derived SBI obtained from  $\gamma^{\text{Avg}}$  and  $\gamma^{\text{PCA}}$ , respectively (Figure 10). As shown in the left panels, the conventional 2PCF-based SBI shows little improvement from PCA denoising, as the process primarily enhances non-Gaussian components that are not effectively captured by the 2PCF method. In contrast, the ML-derived SBI (right panels) benefits substantially from PCA denoising, achieving a 25.7% in-

crease in constraining power and demonstrating its effectiveness in strengthening parameter inference. Overall, compared with the traditional 2PCF method, the combination of PCA denoising and ML-based feature extraction further boosts the constraining power by 36.4%, highlighting the advantage of integrating these techniques for improved cosmological inference. The summarizing of the cosmological constraints is listed in Table 1.

## 6. CONCLUSIONS

We have developed a ML-powered framework for shear-to-cosmology inference, motivated by the complementary strengths of simulation-based inference (SBI) and field-level inference (FLI). SBI offers a simple yet powerful approach for posterior estimation, capable of capturing complex, non-Gaussian, and even multimodal parameter distributions. FLI networks can automatically extract informative and compact representations from cosmological fields. By integrating these two techniques, we establish an effective and robust shear-to-cosmology pipeline that harnesses the advantages of both SBI and FLI. This framework operates directly on the shear fields without requiring convergence reconstruction, and comprises three main components: (1) a shear denoising technique to mitigate the noise from intrinsic galaxy shapes, (2) a Transformer-based network for FLI, and (3) a SBI module.

Theoretically, the convergence and shear fields contain equivalent cosmological information. In practice, however, the shear-to-convergence inversion amplifies noise and introduces filtering artifacts, resulting in non-negligible information loss. A shear-based analysis therefore offers a cleaner alternative. To assess its

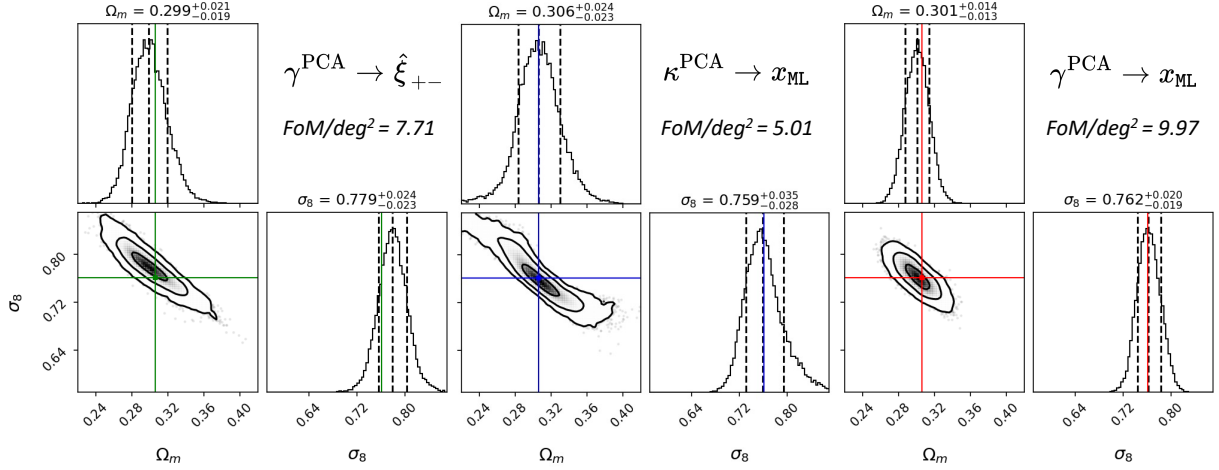


**Figure 9.** Posteriors inferred via SBI using three types of summary statistics over the sky area of  $655.4 \text{ deg}^2$ , with true cosmological parameters  $\Omega_m^{\text{true}} = 0.3062$  and  $\sigma_8^{\text{true}} = 0.7615$ . The left panel shows the posterior using the 2PCF ( $\hat{\xi}_{+-}$ ) of the PCA-denoised shear field ( $\gamma^{\text{PCA}}$ ). The middle panel uses ML-derived features from the convergence field ( $\kappa^{\text{PCA}}$ ), reconstructed from  $\gamma^{\text{PCA}}$  via the KS method. The right panel uses ML-derived features directly extracted from  $\gamma^{\text{PCA}}$ . Based on the values of  $\text{FoM}/\text{deg}^2$ , ML-derived features improve the constraining power by 29.3% over the 2PCFs, and the shear-based method outperforms the kappa-based method by 99.0%.

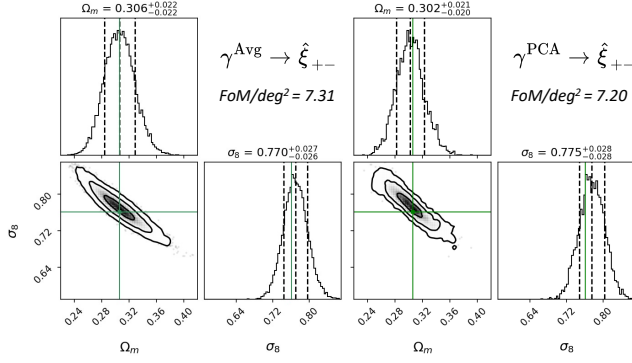
Data	Denoising		Summary Statistics	$\Omega_m$	$\sigma_8$	$\text{FoM}/\text{deg}^2$
	$\mathcal{M}_{\text{sm}}$	PCA				
$\gamma^{\text{Avg}}$	✓	—	2PCF	$0.306^{+0.022}_{-0.022}$	$0.770^{+0.027}_{-0.026}$	7.31
			ML-features	$0.317^{+0.018}_{-0.018}$	$0.743^{+0.026}_{-0.024}$	7.93
$\gamma^{\text{PCA}}$	✓	✓	2PCF	$0.302^{+0.021}_{-0.020}$	$0.775^{+0.028}_{-0.028}$	7.20
			ML-features	$0.301^{+0.014}_{-0.013}$	$0.762^{+0.020}_{-0.019}$	<b>9.97</b>
$\kappa^{\text{Avg}}$	✓	—	ML-features	$0.332^{+0.027}_{-0.025}$	$0.717^{+0.028}_{-0.028}$	4.99
$\kappa^{\text{PCA}}$	✓	✓	ML-features	$0.306^{+0.024}_{-0.023}$	$0.759^{+0.035}_{-0.028}$	5.01

**Table 1.** Cosmological constraints from SBI using a CSST-like WL survey covering  $655.4 \text{ deg}^2$ , with the true parameters  $(\Omega_m^{\text{true}}, \sigma_8^{\text{true}}) = (0.3062, 0.7615)$ .

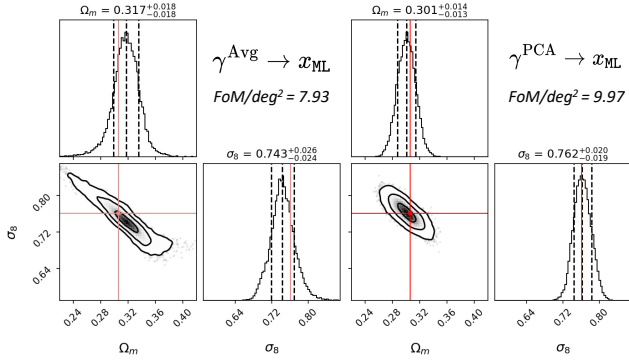
feasibility, we conducted preliminary experiments (not shown here) demonstrating that a Transformer-based U-Net can accurately reconstruct the convergence field from high-S/N shear data, indicating that the network is capable of learning the underlying reconstruction operator. Consequently, even with only shear inputs, the model can, in principle, recover information comparable to that in the true underlying convergence field. Consistently, SBI posteriors show that shear-based analysis nearly doubles the constraining power relative to the KS-convergence field, confirming that the FLI network does extract more cosmological information directly from shear.

In order to capture information encoded in cosmic evolution, the input to our framework is the multi-

redshift shear fields. In practice, increasing the number of redshift bins, however, reduces the galaxy number density within each bin, making denoising essential for multi-redshift WL analyses. Recent studies have applied machine-learning-based denoising methods to WL mass maps (M. Shirasaki et al. 2021; S. D. Aoyama et al. 2025). For shear-based analyses, we instead adopt PCA denoising along the redshift direction, a blind, training-free technique, to suppress noise while preserving the redshift evolution of the shear signal. To assess its impact, we evaluate the effect of PCA denoising using two types of summary statistics within the SBI framework: the 2PCFs and ML-derived features. For the 2PCF-based SBI, the improvement brought by PCA denoising is negligible. In contrast, when using ML-derived



(a) SBI Posteriors using shear 2PCF



(b) SBI Posteriors using ML-derived feature

**Figure 10.** Comparison of SBI posteriors obtained from  $\gamma^{\text{Avg}}$  and  $\gamma^{\text{PCA}}$  over  $655.4 \text{ deg}^2$ , highlighting the impact of PCA denoising on two types of summary statistics: the 2PCFs ( $\xi_{+-}$ ) and ML-derived features ( $x_{\text{ML}}$ ). Based on  $\text{FoM}/\text{deg}^2$ , PCA denoising improves the constraining power by 25.7% when using ML-derived features.

features, PCA denoising results in a 25.7% increase in constraining power. This demonstrates that the PCA-denoised shear fields retain richer cosmological information, predominantly non-Gaussian components, which are effectively exploited by the ML-derived features but not by the traditional 2PCF analysis.

Several aspects of this work warrant further in-depth investigation. Weak lensing analyses have traditionally relied on the convergence field, reconstructed using methods such as Kaiser–Squires algorithm (N. Kaiser & G. Squires 1993), Bayesian forward modeling (J. Alsing et al. 2016), Wiener filtering (N. Jeffrey et al. 2018), wavelet-based techniques (J.-L. Starck et al. 2006; M. Gatti et al. 2025), prior-free maximum likelihood methods (Y. Shi et al. 2024, 2025), machine learning approaches (N. Jeffrey et al. 2020; M. Shirasaki & S. Ikeda 2024), among others. We have employed only the basic KS algorithm for convergence reconstruction in this work, and a systematic comparison between shear-based results and those from alternative reconstruction meth-

ods remains necessary. The potential systematic biases from the denoising procedure remain to be fully assessed. The blind denoising method itself also has room for improvement, for instance through wavelet-based techniques that better separate large- and small-scale structures. The synergy between map-level denoising and redshift-direction denoising could be promising, but requires more significant computational power, thus we leave it for future studies. In addition, due to computational limitations, both the angular resolution and the effective sky area of our input data are significantly lower than those expected for Stage-IV WL surveys. Moreover, many systematic effects are not accounted for in this preliminary study, including PSF effects, intrinsic alignments, source clustering, shear measurement biases, and other observational systematics. To address these limitations, the next step is to construct a suite of mock cosmic fields, including spectroscopic and photometric galaxy catalogs along with the corresponding weak-lensing fields, using high-resolution N-body simulations, partial-sky ray-tracing techniques, and realistic galaxy-image simulations.

In conclusion, we present a unified machine learning framework that integrates FLI and SBI for direct shear-to-cosmology mapping. By combining PCA denoising, a transformer-driven feature extractor, and SBI posterior estimation, our approach enables accurate and efficient cosmological inference directly from shear fields. The results demonstrate that PCA denoising enhances the recovery of non-Gaussian information, while the Transformer-based network effectively captures cosmological signals beyond the reach of shear two-point analyses. These findings highlight the potential of ML-powered hybrid FLI–SBI frameworks to fully exploit the statistical power of weak lensing data, paving the way for more precise and information-rich cosmological parameter estimation in current and future surveys.

## ACKNOWLEDGMENTS

This work was supported by National Key R&D Program of China (2022YFF0503403), National Natural Science Foundation of China (12533008, 12503010, 12203084, 12573006, 12473097), China Manned Space Program (CMS-CSST-2021-(A02, A03, B01), CMS-CSST-2025-(A03, A05)), Postdoctoral Fellowship Program of CPSF (GZC20252089), Guangdong Basic and Applied Basic Research Foundation (2024A1515012309).

*Software:* TreeCorr (M. Jarvis et al. 2004; M. Jarvis 2015), DORIAN (F. Ferlito et al. 2024), PyTorch (A.



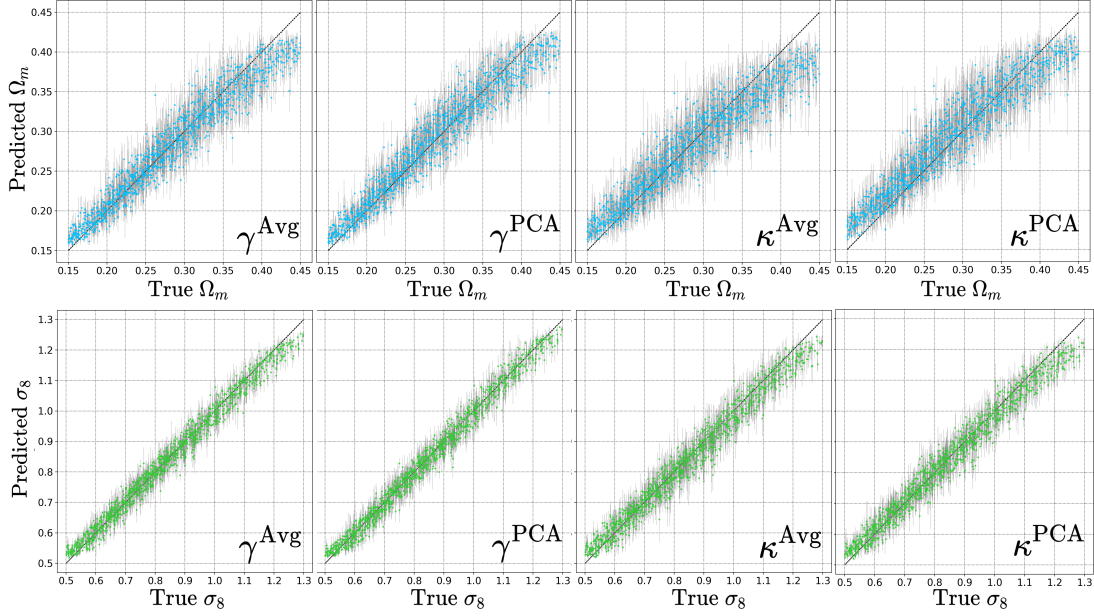


**Figure A1.** Predictions of  $\Omega_m$  and  $\sigma_8$  directly from networks trained and tested on four types of input data: ( $\gamma^{\text{Avg}}$ ,  $\gamma^{\text{PCA}}$ ,  $\kappa^{\text{Avg}}$ ,  $\kappa^{\text{PCA}}$ ). For both shear- and convergence-based inputs, the networks share the same architecture (Figure 1) but are trained independently. Each point, evaluated on the test set, denotes the average prediction over 4 sky groups (covering 655.36 deg<sup>2</sup>) within the same cosmology, with error bars indicating the standard deviation. Dashed lines mark the true parameter values.

Paszke et al. 2019), sbi (A. Tejero-Cantero et al. 2020), HEALPix/healpy (K. M. Górski et al. 2005; A. Zonca et al. 2019), NumPy (S. Van Der Walt et al. 2011; C. R. Harris et al. 2020), OpenMPI (E. Gabriel et al. 2004),

mpi4py (L. Dalcin & Y.-L. L. Fang 2021), SciPy (P. Virtanen et al. 2020), Astropy (T. P. Astropy Collaboration et al. 2013; A. M. Astropy Collaboration et al. 2018, 2022), h5py (A. Collette 2013), Matplotlib (J. D. Hunter 2007), corner (D. Foreman-Mackey 2016)

## APPENDIX

## REFERENCES

- Aihara, H., Arimoto, N., Armstrong, R., et al. 2018, PASJ, 70, S4, doi: [10.1093/pasj/psx066](https://doi.org/10.1093/pasj/psx066)
- Alonso, D., Bull, P., Ferreira, P. G., & Santos, M. G. 2015, MNRAS, 447, 400, doi: [10.1093/mnras/stu2474](https://doi.org/10.1093/mnras/stu2474)
- Alsing, J., Heavens, A., Jaffe, A. H., et al. 2016, MNRAS, 455, 4452, doi: [10.1093/mnras/stv2501](https://doi.org/10.1093/mnras/stv2501)
- Aoyama, S. D., Osato, K., & Shirasaki, M. 2025, arXiv e-prints, arXiv:2505.00345, doi: [10.48550/arXiv.2505.00345](https://doi.org/10.48550/arXiv.2505.00345)
- Astropy Collaboration, Price-Whelan, A. M., Sipőcz, B., Günther, H., et al. 2018, The Astronomical Journal, 156, 123
- Astropy Collaboration, Price-Whelan, A. M., Lim, P. L., Earl, N., et al. 2022, The Astrophysical Journal, 935, 167
- Astropy Collaboration, Robitaille, T. P., Tollerud, E. J., Greenfield, P., et al. 2013, Astronomy & Astrophysics, 558, A33
- Benjamin, J., Van Waerbeke, L., Heymans, C., et al. 2013, MNRAS, 431, 1547, doi: [10.1093/mnras/stt276](https://doi.org/10.1093/mnras/stt276)
- Bernstein, G. M. 2009, ApJ, 695, 652, doi: [10.1088/0004-637X/695/1/652](https://doi.org/10.1088/0004-637X/695/1/652)
- Blake, C., Amon, A., Asgari, M., et al. 2020, A&A, 642, A158, doi: [10.1051/0004-6361/202038505](https://doi.org/10.1051/0004-6361/202038505)
- Boelts, J., Deistler, M., Gloeckler, M., et al. 2024, arXiv preprint arXiv:2411.17337
- Cao, Y., Gong, Y., Meng, X.-M., et al. 2018, MNRAS, 480, 2178, doi: [10.1093/mnras/sty1980](https://doi.org/10.1093/mnras/sty1980)
- Cheng, S., Marques, G. A., Grandón, D., et al. 2025, JCAP, 2025, 006, doi: [10.1088/1475-7516/2025/01/006](https://doi.org/10.1088/1475-7516/2025/01/006)

- Cheng, S., Ting, Y.-S., Ménard, B., & Bruna, J. 2020, MNRAS, 499, 5902, doi: [10.1093/mnras/staa3165](https://doi.org/10.1093/mnras/staa3165)
- Collette, A. 2013, Python and HDF5 (O'Reilly)
- Cranmer, K., Brehmer, J., & Louppe, G. 2020, Proceedings of the National Academy of Science, 117, 30055, doi: [10.1073/pnas.1912789117](https://doi.org/10.1073/pnas.1912789117)
- CSST Collaboration, Gong, Y., Miao, H., et al. 2025, arXiv e-prints, arXiv:2507.04618, doi: [10.48550/arXiv.2507.04618](https://doi.org/10.48550/arXiv.2507.04618)
- Dalcin, L., & Fang, Y.-L. L. 2021, Computing in Science & Engineering, 23, 47
- Dark Energy Survey Collaboration, Abbott, T., Abdalla, F. B., et al. 2016, MNRAS, 460, 1270, doi: [10.1093/mnras/stw641](https://doi.org/10.1093/mnras/stw641)
- Dieleman, S., Willett, K. W., & Dambre, J. 2015, MNRAS, 450, 1441, doi: [10.1093/mnras/stv632](https://doi.org/10.1093/mnras/stv632)
- Dietrich, J. P., & Hartlap, J. 2010, MNRAS, 402, 1049, doi: [10.1111/j.1365-2966.2009.15948.x](https://doi.org/10.1111/j.1365-2966.2009.15948.x)
- Euclid Collaboration, Mellier, Y., Abdurro'uf, et al. 2025, A&A, 697, A1, doi: [10.1051/0004-6361/202450810](https://doi.org/10.1051/0004-6361/202450810)
- Ferlito, F., Davies, C. T., Springel, V., et al. 2024, MNRAS, 533, 3209, doi: [10.1093/mnras/stae2019](https://doi.org/10.1093/mnras/stae2019)
- Fluri, J., Kacprzak, T., Lucchi, A., et al. 2019, PhRvD, 100, 063514, doi: [10.1103/PhysRevD.100.063514](https://doi.org/10.1103/PhysRevD.100.063514)
- Fluri, J., Kacprzak, T., Lucchi, A., et al. 2022, Phys. Rev. D, 105, 083518, doi: [10.1103/PhysRevD.105.083518](https://doi.org/10.1103/PhysRevD.105.083518)
- Foreman-Mackey, D. 2016, The Journal of Open Source Software, 1, 24, doi: [10.21105/joss.00024](https://doi.org/10.21105/joss.00024)
- Gabriel, E., Fagg, G. E., Bosilca, G., et al. 2004, in Recent Advances in Parallel Virtual Machine and Message Passing Interface: 11th European PVM/MPI Users' Group Meeting Budapest, Hungary, September 19-22, 2004. Proceedings 11, Springer, 97–104
- Gatti, M., Anbajagane, D., Chang, C., et al. 2025, arXiv e-prints, arXiv:2509.03798, doi: [10.48550/arXiv.2509.03798](https://doi.org/10.48550/arXiv.2509.03798)
- Gong, Y., Liu, X., Cao, Y., et al. 2019, ApJ, 883, 203, doi: [10.3847/1538-4357/ab391e](https://doi.org/10.3847/1538-4357/ab391e)
- Gong, Y., Miao, H., Zhou, X., et al. 2025, Science China Physics, Mechanics, and Astronomy, 68, 280402, doi: [10.1007/s11433-025-2646-2](https://doi.org/10.1007/s11433-025-2646-2)
- Górski, K. M., Hivon, E., Banday, A. J., et al. 2005, ApJ, 622, 759, doi: [10.1086/427976](https://doi.org/10.1086/427976)
- Harris, C. R., Millman, K. J., Van Der Walt, S. J., et al. 2020, Nature, 585, 357
- Hildebrandt, H., Köhlinger, F., van den Busch, J. L., et al. 2020, A&A, 633, A69, doi: [10.1051/0004-6361/201834878](https://doi.org/10.1051/0004-6361/201834878)
- Hoekstra, H., Yee, H. K. C., & Gladders, M. D. 2004, ApJ, 606, 67, doi: [10.1086/382726](https://doi.org/10.1086/382726)
- Hortúa, H. J., Volpi, R., Marinelli, D., & Malagò, L. 2020, PhRvD, 102, 103509, doi: [10.1103/PhysRevD.102.103509](https://doi.org/10.1103/PhysRevD.102.103509)
- Hu, W. 1999, ApJL, 522, L21, doi: [10.1086/312210](https://doi.org/10.1086/312210)
- Hunter, J. D. 2007, Computing in science & engineering, 9, 90
- Ivezić, Ž., Kahn, S. M., Tyson, J. A., et al. 2019, ApJ, 873, 111, doi: [10.3847/1538-4357/ab042c](https://doi.org/10.3847/1538-4357/ab042c)
- Jarvis, M. 2015, Astrophysics Source Code Library, record ascl:1508.007
- Jarvis, M., Bernstein, G., & Jain, B. 2004, MNRAS, 352, 338, doi: [10.1111/j.1365-2966.2004.07926.x](https://doi.org/10.1111/j.1365-2966.2004.07926.x)
- Jeffrey, N., Lanusse, F., Lahav, O., & Starck, J.-L. 2020, MNRAS, 492, 5023, doi: [10.1093/mnras/staa127](https://doi.org/10.1093/mnras/staa127)
- Jeffrey, N., Abdalla, F. B., Lahav, O., et al. 2018, MNRAS, 479, 2871, doi: [10.1093/mnras/sty1252](https://doi.org/10.1093/mnras/sty1252)
- Kacprzak, T., Fluri, J., Schneider, A., Refregier, A., & Stadel, J. 2022, arXiv e-prints, arXiv:2209.04662, <https://arxiv.org/abs/2209.04662>
- Kaiser, N., & Squires, G. 1993, ApJ, 404, 441, doi: [10.1086/172297](https://doi.org/10.1086/172297)
- Kilbinger, M. 2015, Reports on Progress in Physics, 78, 086901, doi: [10.1088/0034-4885/78/8/086901](https://doi.org/10.1088/0034-4885/78/8/086901)
- Kratochvil, J. M., Lim, E. A., Wang, S., et al. 2012, PhRvD, 85, 103513, doi: [10.1103/PhysRevD.85.103513](https://doi.org/10.1103/PhysRevD.85.103513)
- Leclercq, F. 2025, arXiv preprint arXiv:2509.13435
- Leclercq, F., & Heavens, A. 2021, MNRAS, 506, L85, doi: [10.1093/mnras/rlab081](https://doi.org/10.1093/mnras/rlab081)
- Lemos, P., Cranmer, M., Abidi, M., et al. 2023, Machine Learning: Science and Technology, 4, 01LT01, doi: [10.1088/2632-2153/acbb53](https://doi.org/10.1088/2632-2153/acbb53)
- Liu, J., & Haiman, Z. 2016, PhRvD, 94, 043533, doi: [10.1103/PhysRevD.94.043533](https://doi.org/10.1103/PhysRevD.94.043533)
- Liu, T., Quan, Y., Su, Y., et al. 2025, Nature Astronomy, 9, 608, doi: [10.1038/s41550-025-02484-z](https://doi.org/10.1038/s41550-025-02484-z)
- Liu, Z., Zhang, J., Li, H., Shen, Z., & Liu, C. 2024, Science China Physics, Mechanics, and Astronomy, 67, 270413, doi: [10.1007/s11433-024-2379-0](https://doi.org/10.1007/s11433-024-2379-0)
- Lu, T., Haiman, Z., & Li, X. 2023, MNRAS, 521, 2050, doi: [10.1093/mnras/stad686](https://doi.org/10.1093/mnras/stad686)
- Mandelbaum, R. 2018, ARA&A, 56, 393, doi: [10.1146/annurev-astro-081817-051928](https://doi.org/10.1146/annurev-astro-081817-051928)
- Massey, R., Rhodes, J., Ellis, R., et al. 2007, Nature, 445, 286, doi: [10.1038/nature05497](https://doi.org/10.1038/nature05497)
- Meneghetti, M. 2022, Introduction to Gravitational Lensing: With Python Examples
- Min, Z., Xiao, X., Ding, J., et al. 2024, PhRvD, 110, 063531, doi: [10.1103/PhysRevD.110.063531](https://doi.org/10.1103/PhysRevD.110.063531)
- Oguri, M., Miyazaki, S., Hikage, C., et al. 2018, PASJ, 70, S26, doi: [10.1093/pasj/psx070](https://doi.org/10.1093/pasj/psx070)

- Padilla, L. E., Tellez, L. O., Escamilla, L. A., & Vazquez, J. A. 2021, *Universe*, 7, 213, doi: [10.3390/universe7070213](https://doi.org/10.3390/universe7070213)
- Paszke, A., Gross, S., Massa, F., et al. 2019, arXiv e-prints, arXiv:1912.01703, doi: [10.48550/arXiv.1912.01703](https://doi.org/10.48550/arXiv.1912.01703)
- Petri, A., Haiman, Z., Hui, L., May, M., & Kratochvil, J. M. 2013, *PhRvD*, 88, 123002, doi: [10.1103/PhysRevD.88.123002](https://doi.org/10.1103/PhysRevD.88.123002)
- Petrillo, C. E., Tortora, C., Chatterjee, S., et al. 2017, *MNRAS*, 472, 1129, doi: [10.1093/mnras/stx2052](https://doi.org/10.1093/mnras/stx2052)
- Planck Collaboration, Aghanim, N., Akrami, Y., et al. 2020, *A&A*, 641, A6, doi: [10.1051/0004-6361/201833910](https://doi.org/10.1051/0004-6361/201833910)
- Schawinski, K., Zhang, C., Zhang, H., Fowler, L., & Santhanam, G. K. 2017, *MNRAS*, 467, L110, doi: [10.1093/mnrasl/slx008](https://doi.org/10.1093/mnrasl/slx008)
- Schneider, P., van Waerbeke, L., Kilbinger, M., & Mellier, Y. 2002, *A&A*, 396, 1, doi: [10.1051/0004-6361:20021341](https://doi.org/10.1051/0004-6361:20021341)
- Schrabback, T., Hartlap, J., Joachimi, B., et al. 2010, *A&A*, 516, A63, doi: [10.1051/0004-6361/200913577](https://doi.org/10.1051/0004-6361/200913577)
- Shan, H., Kneib, J.-P., Tao, C., et al. 2012, *ApJ*, 748, 56, doi: [10.1088/0004-637X/748/1/56](https://doi.org/10.1088/0004-637X/748/1/56)
- Shan, H., Liu, X., Hildebrandt, H., et al. 2018, *MNRAS*, 474, 1116, doi: [10.1093/mnras/stx2837](https://doi.org/10.1093/mnras/stx2837)
- Shan, H. Y., Kneib, J.-P., Comparat, J., et al. 2014, *MNRAS*, 442, 2534, doi: [10.1093/mnras/stu1040](https://doi.org/10.1093/mnras/stu1040)
- Shi, Y., Zhang, P., Deng, F., et al. 2025, *JCAP*, 2025, 038, doi: [10.1088/1475-7516/2025/07/038](https://doi.org/10.1088/1475-7516/2025/07/038)
- Shi, Y., Zhang, P., Sun, Z., & Wang, Y. 2024, *PhRvD*, 109, 123530, doi: [10.1103/PhysRevD.109.123530](https://doi.org/10.1103/PhysRevD.109.123530)
- Shirasaki, M., & Ikeda, S. 2024, *The Open Journal of Astrophysics*, 7, 42, doi: [10.33232/001c.118104](https://doi.org/10.33232/001c.118104)
- Shirasaki, M., Moriwaki, K., Oogi, T., et al. 2021, *MNRAS*, 504, 1825, doi: [10.1093/mnras/stab982](https://doi.org/10.1093/mnras/stab982)
- Spergel, D., Gehrels, N., Baltay, C., et al. 2015, arXiv e-prints, arXiv:1503.03757, doi: [10.48550/arXiv.1503.03757](https://doi.org/10.48550/arXiv.1503.03757)
- Starck, J.-L., Pires, S., & Réfrégier, A. 2006, *A&A*, 451, 1139, doi: [10.1051/0004-6361:20052997](https://doi.org/10.1051/0004-6361:20052997)
- Stopyra, S., Peiris, H. V., Pontzen, A., Jasche, J., & Lavaux, G. 2024, *MNRAS*, 527, 1244, doi: [10.1093/mnras/stad3170](https://doi.org/10.1093/mnras/stad3170)
- Su, C., Shan, H., Zhao, C., Xu, W., & Zhang, J. 2025, *A&A*, 699, A174, doi: [10.1051/0004-6361/202555237](https://doi.org/10.1051/0004-6361/202555237)
- Tang, J. Y., & Fan, Z. H. 2005, *ApJ*, 635, 60, doi: [10.1086/497285](https://doi.org/10.1086/497285)
- Taylor, P. L., & Markovič, K. 2022, *PhRvD*, 106, 063536, doi: [10.1103/PhysRevD.106.063536](https://doi.org/10.1103/PhysRevD.106.063536)
- Tejero-Cantero, A., Boelts, J., Deistler, M., et al. 2020, *Journal of Open Source Software*, 5, 2505, doi: [10.21105/joss.02505](https://doi.org/10.21105/joss.02505)
- Van Der Walt, S., Colbert, S. C., & Varoquaux, G. 2011, *Computing in science & engineering*, 13, 22
- Van Waerbeke, L., Benjamin, J., Erben, T., et al. 2013, *MNRAS*, 433, 3373, doi: [10.1093/mnras/stt971](https://doi.org/10.1093/mnras/stt971)
- Virtanen, P., Gommers, R., Oliphant, T. E., et al. 2020, *Nature methods*, 17, 261
- Wu, Y., Li, N., Shan, H.-Y., et al. 2025, *Research in Astronomy and Astrophysics*, 25, 125003, doi: [10.1088/1674-4527/ae088a](https://doi.org/10.1088/1674-4527/ae088a)
- Yao, J., Shan, H., Zhang, P., et al. 2023, *A&A*, 673, A111, doi: [10.1051/0004-6361/202346020](https://doi.org/10.1051/0004-6361/202346020)
- Yao, J., Shan, H., Li, R., et al. 2024, *MNRAS*, 527, 5206, doi: [10.1093/mnras/stad3563](https://doi.org/10.1093/mnras/stad3563)
- Zeghal, J., Lanzieri, D., Lanusse, F., et al. 2025, *A&A*, 699, A327, doi: [10.1051/0004-6361/202452410](https://doi.org/10.1051/0004-6361/202452410)
- Zhan, H. 2021, *Chinese Science Bulletin (Chinese Version)*, 66, 1290
- Zhang, Z., Shan, H., Li, N., et al. 2024, *A&A*, 683, A209, doi: [10.1051/0004-6361/202345903](https://doi.org/10.1051/0004-6361/202345903)
- Zhong, F., Luo, R., Napolitano, N. R., et al. 2025, *ApJS*, 277, 12, doi: [10.3847/1538-4365/ada609](https://doi.org/10.3847/1538-4365/ada609)
- Zonca, A., Singer, L., Lenz, D., et al. 2019, *Journal of Open Source Software*, 4, 1298, doi: [10.21105/joss.01298](https://doi.org/10.21105/joss.01298)